Simultaneous Identification of Multiple Unexploded Ordnance Using Electromagnetic Induction Sensors

Tomasz M. Grzegorczyk, *Senior Member, IEEE*, Benjamin E. Barrowes, *Member, IEEE*, Fridon Shubitidze, *Member, IEEE*, Juan Pablo Fernández, and Kevin O'Neill, *Member, IEEE*

Abstract—The simultaneous detection and identification of multiple targets using electromagnetic induction (EMI) time-domain sensors remains a challenge due to the fast decay of the magnetic field with sensor-target distance. For example, the signal from a weak yet shallow target or clutter item can overshadow that from a much larger yet deeper unexploded ordnance (UXO), potentially resulting in erroneous localization and/or identification. We propose, in this paper, a method based on the Gauss–Newton algorithm for the inversion of multiple targets within the field of view of sensors operating at EMI frequencies (tens of hertz to a few hundred kilohertz). In order to minimize the number of unknowns to invert for, the polarizability tensor is written as a time-independent orientation matrix multiplied by a time-dependent diagonal intrinsic polarizability tensor. Similarly, position is supposed to be time independent so that both position and orientation angles are inverted only once using all time channels collected by the instrument. Moreover, using the dipole approximation, we are able to compute the Jacobian in closed form for instruments with either square or circular primary field coils, thus contributing to the speed of the algorithm. Validating results are shown based on the measurement data collected with two EMI sensors on various types of UXO.

Index Terms—Electromagnetic induction, Gauss–Newton method, subsurface sensing, unexploded ordnance (UXO).

I. INTRODUCTION

NUMEROUS military campaigns and extensive warfare practice over the last decades have left millions of acres of land contaminated worldwide with unexploded ordnance (UXO), projectiles with explosive cores, and metallic shells that did not explode upon impact and penetrated into the ground. The cleaning of these fields is currently a daunting and hugely expensive task that consumes a budget of several million dollars in the United States alone. This prohibitively large cost is due to a very large false-alarm rate associated with the detection of UXO with current remote sensing technologies. Differentiating between unexploded and exploded ordnance is a technological challenge that is yet to be overcome in realistic field situations, where clutter and/or geological factors can significantly jam the signals used by remote sensing algorithms. As a result, current cleaning campaigns are based on overly simple metal detection schemes with little discrimination involved, yielding huge time-consuming and expensive campaigns which result most of the time in the excavation of harmless objects.

In parallel, researchers have spent decades investigating technologies and refining algorithms to detect and discriminate metallic subsurface objects better. For example, radar sensors operating in the microwave regime, which have been so successful when pointing to the sky, have been turned upside down to send and receive signals into and from the ground. Advanced signal processing techniques have proven the usefulness of this approach [1], [2] but also revealed its limitations due to the variations in soil surfaces and volume compositions which quickly obscure the signatures of the subsurface targets. As an alternative, electromagnetic induction (EMI) which utilizes magnetic fields at much lower frequencies (from tens of hertz to a few hundred kilohertz) has proven to be remarkably robust. The associated magnetoquasi-static regime ensures that displacement currents are negligible compared to conduction currents in the metallic targets. The soil, assumed here to be nonmagnetic and nonconductive, is transparent so that the UXO can be simply considered in free space. Various models have been proposed, from the simple but effective dipole model [3]–[6] to more elaborated theoretical studies on canonical shapes [7]–[9], as well as more flexible numerical models [10], [11]. The purpose of these various techniques is to improve the discrimination capabilities of UXO in realistic environments [12]–[15].

A major drawback of the EMI regime, however, is its sharp field decay approximately as $1/r^3$ at large distances compared to the primary coil size, with r being the target-sensor distance, which makes it difficult to use EMI frequencies at ranges beyond a few times the size of the coils or when identifying multiple UXO in close proximity to one another as well as in close proximity to large clutter items. For example, even a small but shallow metal object can overshadow the signal of a deeper UXO producing an erroneous classification. A related problem occurs when targets of similar sizes are buried alongside one another at comparable depths [16]. In both situations, the detection and identification can be considerably

improved by considering a multitarget configuration, whereby multiple time signatures are simultaneously inverted for and used in the decision scheme. One of the first attempt along this direction collaboratively used EMI and radar signals [17], [18]. This approach, however, revealed to be both time consuming and costly due to the combination of two hardware and two analysis algorithms. Other attempts concentrated on using only EMI data with signal processing techniques for sources separation [19]. Successful results were reported on synthetic data (i.e., computer generated), while more validation is expected using real UXO and EMI sensors. Similarly, an independent component analysis revealed the possibility of extracting the signature of a UXO in the presence of multiple clutter items, but the method concentrated on the specific situation of known UXO, i.e., a known signature which had to be extracted from a sum of multiple signatures [20]. More recently, positions, orientations, and time-dependent polarizabilities were inverted on two-target configurations from both synthetic as well as sensor data [21]. The method, based on a multistart search and separation of the linear and nonlinear parameters, was shown to yield good agreement with ground truth. However, as the authors point out, the strong nonlinearity of the problem required a good initial guess, which was provided by sampling a region of interest. This requirement could be alleviated by using a multiple signal classification approach [22], [23] for position estimation (nonlinear part) followed by a direct solution of the polarizabilities (linear part) using either a least square method [24], a Kalman filter approach [25], or other. Yet, this approach presents some limitation when monostatic data are used in the inversion process.

Trying to alleviate some of these pitfalls, we propose in this paper an algorithm significantly improved compared to our previous work [26], with the following new features: factorization of the time-independent orientation angles from the time-dependent unknown vector, incremental step size in the Gauss–Newton algorithm, analytical computation of the Jacobian matrix for square and circular primary field coils, and solution selection. The resulting new algorithm shows robustness to initial conditions that removes the need of user-defined regions of interest, numerical stability that reduces the number of realizations necessary to filter out local minima solutions, and computational speed. The method is here extensively validated using the measured data from two types of EMI sensors (man portable vector (MPV) and Time-domain Electro-Magnetic Multi-sensor Towed Array Detection System (TEMTADS)) on a variety of UXO.

II. PROBLEM CONFIGURATION AND EMI SENSORS

We consider the problem illustrated in Fig. 1, whereby a sensor at position $\bar{r}_s$ illuminates multiple targets described by their positions $\bar{r}_\ell = \hat{x} x_\ell + \hat{y} y_\ell + \hat{z} z_\ell$, elevations θ_ℓ, and azimuths ϕ_ℓ, where $l = 1, \ldots, N$ ($N = 3$ is shown in the figure). We suppose all N targets to be bodies of revolution, modeled as a three-axis dipole with parameters $\bar{r}_\ell$, θ_ℓ, ϕ_ℓ and intrinsic polarizabilities $\bar{\bar{\beta}}_\ell$ [see subsequent (5c)]. The transmitter and receiver sensors are incorporated into our algorithm to closely model the hardware configuration of either the TEMTADS [27],
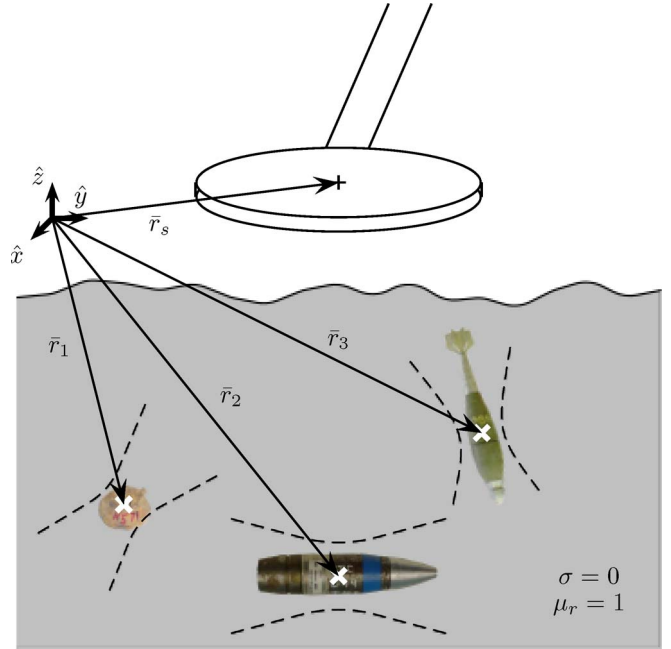

Fig. 1. Problem configuration: an EMI sensor surveys an area where N targets are buried ($N = 3$ in the figure). The unknowns of the problem are the target (intrinsic) polarizabilities themselves as well as their positions $\bar{r}_\ell$ and orientations (θ_ℓ, ϕ_ℓ). The soil is supposed to be nonconductive ($\sigma = 0$) and nonpermeable ($\mu_r = 1$).

[28] or the MPV [29] instruments. The TEMTADS is composed of an array of 5×5 horizontal square receiver sensors separated by 40 cm (center to center) in the (xy) plane and collects z components of the secondary magnetic field induced by the target. Each sensor is composed of a square transmitting coil (side dimension: 35 cm) and a cocentered square receiving coil (side dimension: 25 cm) which are time decoupled: During the first half of the cycle, the transmitting coils emit a primary field which excites all metals in its vicinity, whereas during the second half of the cycle, the receiving coil measures the derivative of the flux generated by all ringing metal objects. The hardware electronics integrates the flux to yield a quantity proportional to the magnetic field which is measured typically after the first 100 μs to let the secondary field of all metals but targets die away. The targets themselves typically ring for a few microseconds so that measurements are gathered until about 25 ms logarithmically sampled in 120 time channels. Measurements can be performed in either a monostatic mode, in which case all the 25 sensors sequentially transmit and receive yielding 25 data points, or in a bistatic mode in which case each transmitter fires sequentially and measurements are gathered by all 25 receivers yielding 625 data points. We model the transmitters as square current loops whose primary field can be written as the addition of four sections of straight wire which all carry a unit constant current. The primary field from each wire is given by

$$\bar{H}^{\text{wire}} = \frac{\hat{s}}{4\pi|\bar{s}|}(\hat{r}_1 - \hat{r}_2) \cdot \hat{r}_{12} \tag{1}$$

where a hat denotes a unit vector and a bar denotes a regular vector, $\hat{r}_1$ and $\hat{r}_2$ are the unitary vectors between each extremity

of the straight wires and the observation point, $\bar{r}_{12} = \bar{r}_2 - \bar{r}_1$, and $\bar{s} = \hat{r}_{12} \times \bar{r}_1$. The received signal at each receiver is simply computed by integrating the secondary magnetic field over the surface of the corresponding receiving square coil.

The MPV [29] sensor is very different from the TEMTADS in that it is much smaller and lighter. It uses a pair of coaxial circular transmitting coils (with a radius of 37.5 cm and a vertical separation of 15.6 cm) and a series of five square receiving coils (with side dimensions of 10 cm) which can measure all components of the secondary field. The primary field is modeled as that produced by a circular current loop of radius a and unit current. In the cylindrical coordinate system, the field at (ρ, z) is written as [4], [30]

$$
\begin{aligned}
H_\rho(\rho, z) = &\frac{1}{2\pi} \frac{1}{\sqrt{(a+\rho)^2 + z^2}} \frac{z}{\rho} \\
&\times \left[\frac{a^2 + \rho^2 + z^2}{(\rho - a)^2 + z^2} E(k) - K(k) \right]
\end{aligned}
\tag{2a}
$$

$$
\begin{aligned}
H_z(\rho, z) = &\frac{1}{2\pi} \frac{1}{\sqrt{(a+\rho)^2 + z^2}} \\
&\times \left[\frac{a^2 - \rho^2 - z^2}{(\rho - a)^2 + z^2} E(k) + K(k) \right]
\end{aligned}
\tag{2b}
$$

where $K(k)$ and $E(k)$ are the elliptic integrals of the first and second kind, respectively, with $k^2 = 4a\rho/[(\rho+a)^2 + z^2]$. The received signal is computed by integrating the secondary magnetic field over the surface of the receiving perpendicular square coils. Like for the TEMTADS, measurements are gathered during off-time cycles (when the primary field is turned off), between about 0.4 and 25 ms sampled in 30 time channels. Inherent to its construction, the operating mode of the MPV is a mixture of monostatic and bistatic mode, typically coined multistatic (the receivers are tied to the transmitter but not collocated). Advantages compared to the TEMTADS are its vectorial property and its maneuverability in complex terrain, whereas its disadvantages are its smaller field of view and the necessity of tracking its position and orientation during data acquisition.

III. DATA ANALYSIS

The fast field decay in the EMI regime ensures that near-field effects are confined to a very small volume surrounding the buried target. As a consequence, the secondary field at the sensor location is almost identical to that of a triaxial dipole, for which the magnetic field $\bar{H}$ is given by [4]

$$
\bar{H}(\bar{r}_s) = \frac{1}{4\pi r_{ts}^3} \left[\frac{3\bar{r}_{ts}(\bar{r}_{ts} \cdot \bar{m})}{r_{ts}^2} - \bar{m} \right]
\tag{3}
$$

where $\bar{m} = \hat{x} m_x + \hat{y} m_y + \hat{z} m_z$ is the dipole moment of the target, $\bar{r}_t$ is the target location, $\bar{r}_s$ is the sensor location, $\bar{r}_{ts} = \bar{r}_s - \bar{r}_t$, and $r_{ts} = \|\bar{r}_{ts}\|$. It should be mentioned that the dipole analysis remains to be an approximation which has proven to be accurate in the overwhelming majority of UXO configurations. However, its limitation is particularly obvious with heterogeneous targets or when multiple targets are in very

close proximity to one another, typically within a subcentimeter distance, with one or both targets being ferrous [31]. In this situation, coupling between eddy currents of the two objects can happen at a level sufficient to alter the secondary magnetic field at the receiver location [32]. Such configuration is, however, more theoretical than practical and, to our knowledge, has not been encountered beyond laboratory tests. As a consequence, we suppose here that the separation between the targets is sufficient to ensure that the various UXO respond as independent dipoles with no coupling effects [33]. Within such independent scattering approximation, the magnetic field of N targets located at $\bar{r}_\ell$ ($\ell = 1, \ldots, N$) and with dipole moments $\bar{m}_\ell$ is simply obtained as the algebraic sum of (3)

$$
\bar{H}(\bar{r}_s) = \sum_{\ell=1}^{N} \frac{1}{4\pi r_{\ell s}^3} \left[\frac{3\bar{r}_{\ell s}(\bar{r}_{\ell s} \cdot \bar{m}_\ell)}{r_{\ell s}^2} - \bar{m}_\ell \right].
\tag{4}
$$

Note that we assume N to be known in (4), which is an assumption further discussed in Section IV. The dipole moment $\bar{m}_\ell$ is obtained from the self-polarizability $\bar{\bar{\beta}}_\ell$ of the target along three directions, weighted by the primary field at the target location. If, in addition, the target is rotated with respect to the global reference frame, the rotation angles need to be incorporated. Restricting ourselves to bodies of revolution as most UXO are, the dipole moment $\bar{m}_\ell$ can be written as

$$
\bar{m}_\ell = \bar{\bar{\Lambda}}_\ell^T \cdot \bar{\bar{\beta}}_\ell \cdot \bar{\bar{\Lambda}}_\ell \cdot \bar{H}^{pr}(\bar{r}_\ell)
\tag{5a}
$$

where

$$
\bar{\bar{\Lambda}}_\ell = \begin{pmatrix} \cos\theta_\ell \cos\phi_\ell & \cos\theta_\ell \sin\phi_\ell & -\sin\theta_\ell \\ -\sin\phi_\ell & \cos\phi_\ell & 0 \\ \sin\theta_\ell \cos\phi_\ell & \sin\theta_\ell \sin\phi_\ell & \cos\theta_\ell \end{pmatrix}
\tag{5b}
$$

is the rotation matrix with the angles θ_ℓ and ϕ_ℓ

$$
\bar{\bar{\beta}}_\ell = \begin{pmatrix} \beta_{x_\ell} & 0 & 0 \\ 0 & \beta_{y_\ell} & 0 \\ 0 & 0 & \beta_{z_\ell} \end{pmatrix}
\tag{5c}
$$

where $(\beta_{x_\ell}, \beta_{y_\ell}, \beta_{z_\ell})$ are the time-dependent polarizabilities along the three directions of the reference frame local to the target and $\bar{H}^{pr}(\bar{r}_\ell)$ is the primary field at the target location. Note that the two components of $\bar{\bar{\beta}}_\ell$ are expected to be identical due to the body-of-revolution assumption, even though this property is not enforced in (5c). For example, in a bistatic configuration, the transmitter remains at a unique location, while the receiver spans a series of measurement points. As a consequence, the primary field $\bar{H}^{pr}(\bar{r}_\ell)$ is unique and so is $\bar{m}_\ell$. In a monostatic configuration, however, where the transmitter and receivers are collocated and span together the measurement points, $\bar{H}^{pr}(\bar{r}_\ell)$ varies from point to point and so does $\bar{m}_\ell$. The polarizability tensor $\bar{\bar{\beta}}_\ell$, however, is invariant and can be used by a classifier for each target.

Our inversion algorithm is based on a Gauss–Newton solution of the normal equation assuming that N targets are present in the field of view of the sensor. The simultaneous inversion of the time-independent position, orientation, and time-dependent polarizabilities of the targets is expressed as a least-squares

minimization between the measured field and the predicted field computed from (4). Hence, the unknown vector is written as

$$\mathbf{x} = [\mathbf{a}_1 \ldots \mathbf{a}_\ell \ldots \mathbf{a}_N \ \mathbf{b}_1 \ldots \mathbf{b}_\ell \ldots \mathbf{b}_N]^T \quad (6a)$$

$$\mathbf{a}_\ell = [x_\ell \ y_\ell \ z_\ell \ \theta_\ell \ \phi_\ell]^T \quad (6b)$$

$$\mathbf{b}_\ell = \left[\beta_{x_\ell}^{t_1} \ \beta_{y_\ell}^{t_1} \ \beta_{z_\ell}^{t_1} \ \ldots \ \beta_{x_\ell}^{t_{N_{tc}}} \ \beta_{y_\ell}^{t_{N_{tc}}} \ \beta_{z_\ell}^{t_{N_{tc}}} \right]^T \quad (6c)$$

where t_j $(j = 1, \ldots, N_{tc})$ denotes the time channels and where the superscript T denotes the transpose. Equation (6c) indicates that the algorithm solves for a single position and a single orientation per target, with multiple polarizabilities across the time history of the transmitter for all targets simultaneously. Note that it is also possible to invert for a more general polarizability tensor with six independent elements [21], [34], [35]. Although such approach has been shown to be valid and accurate, it is not adopted here: Inverting a full tensor at each time channel is analogous to inverting for the rotation angles at each time channel. Within a good approximation, however, these angles can be considered time independent so that we factor them out of the polarizability tensor and include them in the time independent part of the minimization vector, thus drastically reducing the number of unknowns to invert for. Note that, similarly, the algorithm inverts for a unique position rather than a time-dependent position at every time channel. Considering the position and angles to be time independent is an approximation justified in practice. Indeed, although various parts of the UXO may respond differently in time, effectively yielding slightly different positions and orientations of the triaxial dipole used to best match the measured secondary field, we have found this effect to be small in the cases considered in this paper: Inverting the positions at every time channel yields similar estimates except at later times when the field values reach the noise level (data not shown).

The task of the minimization algorithm is to estimate the unknown parameter $\mathbf{x}$ so as to minimize the sum of squares

$$\min_{\mathbf{x}} S = \min_{\mathbf{x}} \left(\Delta \bar{H}_z^T \Delta \bar{H}_z \right) \quad (7)$$

where $\Delta \bar{H}_z = (\bar{H}_z^{\text{mea}} - \bar{H}_z)$ with $\bar{H}_z^{\text{mea}}$ and $\bar{H}_z$ being the measured and computed z components of the magnetic field, respectively. If needed, the addition of other components of the magnetic field to the minimization problem is straightforward (e.g., the TEMTADS measures only H_z, whereas the MPV measures all three components). The corresponding normal equation is written as

$$\bar{\bar{J}}_z^T \bar{\bar{J}}_z \cdot \Delta \mathbf{x} = \bar{\bar{J}}_z^T \cdot \Delta \bar{H}_z \quad (8)$$

where $\Delta \mathbf{x} = \mathbf{x}^{i+1} - \mathbf{x}^i$ is the unknown vector which provides the updated quantities of $\mathbf{x}$ at each iteration, i is the iteration number, and $\bar{\bar{J}}_z$ is the Jacobian matrix. The Gauss–Newton update equation is therefore

$$\mathbf{x}^{i+1} = \mathbf{x}^i + \Delta \mathbf{x} = \mathbf{x}^i + \left(\bar{\bar{J}}_z^T \bar{\bar{J}}_z \right)^{-1} \bar{\bar{J}}_z^T \cdot \left(\bar{H}_z^{\text{mea}} - \bar{H}_z \right). \quad (9)$$

The vector notation used on $\bar{H}_z^{\text{mea}}$ and $\bar{H}_z$ refers to the fact that the magnetic field is measured and computed over a series

of K observation points. The Jacobian matrix is, therefore, a block matrix of size $[N_{tc} \times K, N(5 + 3N_{tc})]$ where N_{tc} is the number of time channels. Splitting the Jacobian matrix into time-independent and time-dependent parts, we write

$$\bar{\bar{J}}_z = [\bar{\bar{A}}_z, \bar{\bar{B}}_z] \quad (10)$$

where $\bar{\bar{A}}_z$, of size $[N_{tc} \times K, 5N]$, gathers the derivatives of the computed $\bar{H}_z$ field with respect to the three positions and two angles across all observation points and time channels. Assuming $N = 1$ for the sake of simplicity of notation in this example

$$\bar{\bar{A}}_z = \begin{pmatrix} \bar{\bar{A}}_z^{t_1} \\ \vdots \\ \bar{\bar{A}}_z^{t_j} \\ \vdots \\ \bar{\bar{A}}_z^{t_{N_{tc}}} \end{pmatrix} \quad \text{with} \quad \bar{\bar{A}}_z^{t_j} = \begin{pmatrix} \bar{A}_{z_1}^{t_j} \\ \vdots \\ \bar{A}_{z_\ell}^{t_j} \\ \vdots \\ \bar{A}_{z_K}^{t_j} \end{pmatrix} \quad (11a)$$

$$\bar{A}_{z_\ell}^{t_j} = \left[\frac{\partial}{\partial x_\ell} \ \frac{\partial}{\partial y_\ell} \ \frac{\partial}{\partial z_\ell} \ \frac{\partial}{\partial \theta_\ell} \ \frac{\partial}{\partial \phi_\ell} \right] H_z^{t_j}(\bar{r}_\ell) \quad (11b)$$

where $H_z^{t_j}(\bar{r}_\ell)$ is the z component of the magnetic field obtained from (4) and (5) at time channel t_j. The matrix $\bar{\bar{B}}_z$ is a block diagonal matrix where each block has a size $[N_{tc} \times K, 3N_{tc}]$ (still under the assumption of $N = 1$) and gathers the derivatives of the computed $\bar{H}_z$ field with respect to the three polarizabilities

$$\bar{\bar{B}}_z = \text{diag} \left[\bar{\bar{B}}_z^{t_1}, \ldots, \bar{\bar{B}}_z^{t_j}, \ldots, \bar{\bar{B}}_z^{t_{N_{tc}}} \right] \text{ with } \bar{\bar{B}}_z^{t_j} = \begin{pmatrix} \bar{B}_{z_1}^{t_j} \\ \vdots \\ \bar{B}_{z_\ell}^{t_j} \\ \vdots \\ \bar{B}_{z_K}^{t_j} \end{pmatrix}$$

$$(12a)$$

$$\bar{B}_{z_\ell}^{t_j} = \left[\frac{\partial}{\partial \beta_{x_\ell}} \ \frac{\partial}{\partial \beta_{y_\ell}} \ \frac{\partial}{\partial \beta_{z_\ell}} \right] H_z^{t_j}(\bar{r}_\ell). \quad (12b)$$

The formulation outlined earlier is straightforward to generalize to the case of $N > 1$ as well as when all components of the magnetic field are known by simply stacking the Jacobian matrices and right-hand side vectors corresponding to other components and generalizing the unknown vector $\mathbf{x}$. Note that all the derivatives are straightforward to compute except those with respect to position since they require the derivative of the primary field as well, in view of (5a). This task can still be performed analytically for both the TEMTADS and MPV sensors using (1) and (2) and a precise knowledge of the sensors' geometries, which contributes to the computational efficiency of the algorithm.

The actual implementation of (9) is slightly modified by the addition of a weighting factor $\alpha \leq 1$ in order to control the step size

$$\mathbf{x}^{i+1} = \mathbf{x}^i + \alpha \left(\bar{\bar{J}}_z^T \bar{\bar{J}}_z \right)^{-1} \bar{\bar{J}}_z^T \cdot \left(\bar{H}_z^{\text{mea}} - \bar{H}_z \right). \quad (13)$$

TABLE I
INVERTED POSITIONS OF SINGLE TARGETS USING DATA FROM THE MPV INSTRUMENT. THE TIME SIGNATURES FOR
THE 81 mm AND THE BLU26 ARE SHOWN IN FIG. 2. POSITIONS ARE ROUNDED TO THE CLOSEST INTEGER

Target	Length [mm]	Ground truth					Inverted results				
		[cm]			[degrees]		[cm]			[degrees]	
		x	y	z	θ	ϕ	x	y	z	θ	ϕ
Al sphere		0	22	26	-	-	0	22	29	-	-
Brass sphere		0	22	26	-	-	0	22	28	-	-
Steel sphere		0	22	26	-	-	0	22	28	-	-
81-mm	490	-23	22	52	-18	0	-14	22	50	-20	-10
105-mm	642	-20	22	63	-19	180	-12	23	50	-30	176
BLU26	70.31	0	22	38	0	0	0	22	34	-	-
57-mm	170.47	5	22	55	307	180	4	22	51	310	160
60-mm	245	0	22	51	270	0	0	22	48	260	7

Empirical investigations revealed an increasing importance of α as the number of targets to invert for increased: from practically unnecessary, for $N = 1$, to important, for $N \geq 3$. While further analytical investigations might be necessary to determine the optimal α for each configuration, results reported hereafter have been obtained with $\alpha = 0.5$, which appears to offer a good compromise between accuracy and convergence speed.

IV. INVERSION RESULTS

Despite an extensive validation campaign on synthetic data, we concentrate on and only present here the results from data that have been acquired by real sensors on real UXO. Data have been collected using both the TEMTADS and MPV instruments, and the inversion results are presented in the following two sections on various multitarget configurations. It is important to keep in mind that measurements are performed on real UXO which therefore have certain physical dimensions, whereas the algorithm is inverting for one triaxial dipole per UXO. The location of these equivalent dipoles is not precisely defined: It is close to the center of the target if the latter is buried horizontally (i.e., parallel to the sensor), whereas it migrates toward the tip for vertical targets where one extremity is closer to the sensor than the other. The positions also depend on the composition, geometry, and external features of each target, such as fins, conductive rings, etc. The exact location at which a single triaxial dipole should be located in order to best reproduce the secondary field of a given UXO is therefore not expected to match exactly the positions recorded at the data acquisition stage (which correspond typically to the exact center or exact tip of the UXO). The accuracy of the subsequent results should be judged with these considerations in mind.

A. MPV Data

The MPV is a vectorial multistatic EMI instrument which collects data as it is waved above the surface. Due to its intrinsic portable nature, the trajectory of the MPV as well as its orientation (e.g., pitch, roll, and yaw) needs to be tracked during the entire data acquisition time. The data set thus collected is then converted into components of the magnetic field along three predefined directions and subsequently processed by our algorithm. The results reported hereafter have been obtained using the vectorial information of all five sensors, even though more in depth studies showed that not all carry critical information necessary for proper inversion (data not shown).
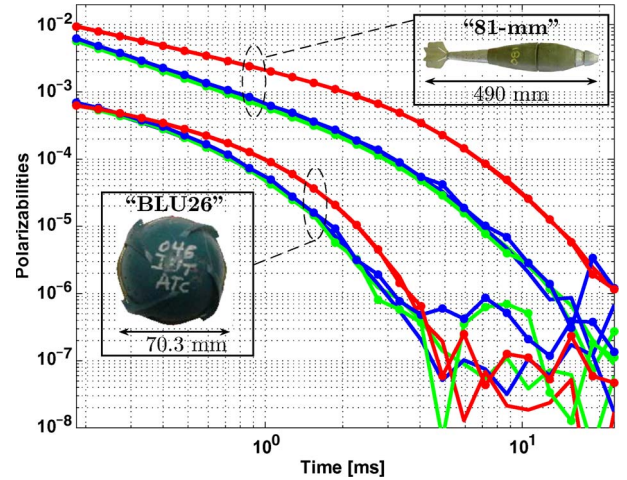

Fig. 2. Time-domain polarizabilities for two types of UXO (81 mm and BLU26) measured and inverted separately from MPV data.

A first series of validating tests of our MPV model was performed on single targets and yielded good results in all the cases considered for both the positions, orientations, and time-dependent polarizabilities. Table I lists a few cases with the corresponding inverted positions and orientations which show a reasonable agreement with the ground truth. We recall here that the ground truth values typically correspond to distances to the center of the UXO, which might be a few centimeters away from the optimized location of an equivalent dipole. For example, elevation of the 60-mm UXO was set to $\theta = 270°$, which corresponds to the target being perfectly flat. A simple correction to the inverted depth for this case therefore demands to account for the half width of the target, i.e., 30 mm, which augments the inverted depth from 48 to 51 cm, which is in good agreement with the ground truth. Corrections to other targets are not as straightforward to incorporate because of the nontrivial elevations. The largest deviation in depth amounts to 10 cm and occurs with the 105 mm with $\theta = -19°$. The small elevation indicates that the target is close to vertical so that an important deviation between the center position and the location of the equivalent dipole is expected, particularly because this target is very long. In addition to the mismatch between the center of the target and the location of its equivalent dipole, part of the discrepancies in Table I can also be attributed to measurement and instrument noise, while, yet, another part could be due to algorithmic inaccuracies (for example, due to a too small data set to optimize the unknown vector to a desired level of accuracy). The overall good results, however,

TABLE II
INVERSION RESULTS ON TWO-TARGET CONFIGURATIONS FROM DATA COLLECTED
BY THE MPV SENSOR. POSITIONS ARE ROUNDED TO THE CLOSEST INTEGER

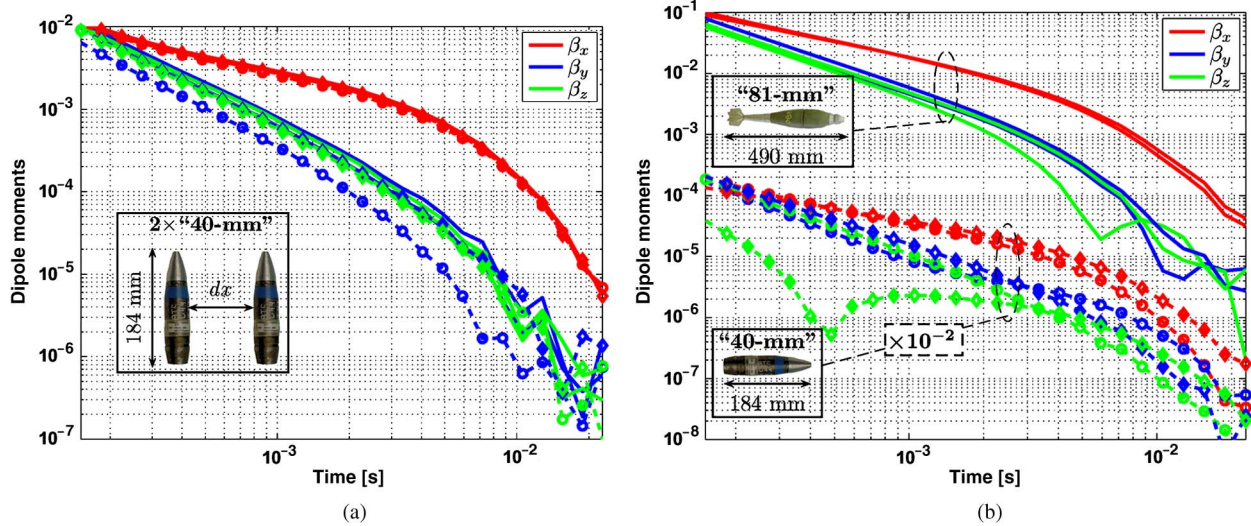| UXO	Truth [cm]						Inverted [cm]					
	x_1	y_1	z_1	x_2	y_2	z_2	x_1	y_1	z_1	x_2	y_2	z_2
40-mm & 40-mm	0	0	40	25	0	40	2	−1	40	23	0	38
40-mm & 40-mm	0	0	40	40	0	40	1	−1	39	40	−2	39
81-mm & 40-mm	0	0	40	25	0	40	0	0	42	18	0	40
81-mm & 40-mm	0	0	65	25	0	40	0	0	43	22	0	38

Fig. 3.   Time-domain polarizabilities for two two-target configurations measured by the MPV. Inverted positions are summarized in Table II. (a) Two 40-mm UXO inverted in two configurations: $(x_2 - x_1, z_2 - z_1) = (dx, dz) = (25, 0)$ and $(40, 0)$ cm. (Circle marks) The visibly weaker components correspond to $dx = 25$ cm. (b) 81-mm and 40-mm UXO inverted in two configurations: $(x_2 - x_1, z_2 - z_1) = (dx, dz) = (25, 0)$ and $(25, 25)$ cm. (Diamond marks) The weaker and dipping component corresponds to $dz = 25$ cm.

suggest that the algorithm is effective at inverting MPV data. This conclusion is also supported by the time-dependent polarizabilities obtained for these cases; a subset of which is shown in Fig. 2. As expected, the 81-mm UXO shows one polarizability element consistently stronger than the other two which are almost identical and reveal a geometric azimuthal symmetry. The BLU26 exhibits similar characteristics, but the three polarizabilities are closer to each other due to the close to spherical shape of this UXO (see inset).

Two-target results present mitigated yet consistent results within the data set available to us. Two configurations were analyzed: that of two 40-mm UXO at the same depth and that of a 40 mm along with 81-mm UXO at varying depths, both cases for different lateral separations. Inverted positions, summarized in Table II, indicated a good performance when the targets are at the same depth, with yet improved accuracy for larger lateral separations as intuitively expected. This is evident from the inverted polarizabilities of the two 40-mm targets, shown in Fig. 3(a): While the four strong components (two targets in two configurations) are almost identical in both cases, one of the weak components is slightly underestimated for $dx = 25$ cm (circle marks). The good performance at identical depth is somewhat maintained with the two different targets, despite a small error in the inverted lateral separation which can be mostly attributed to the physical width of the targets. Incorporating this correction of about 6 cm, the inverted separation would be about 21 cm instead of the measured 25 cm. The overall results worsen, however, when the two targets are at

different depths, with z_2 in Table II often underestimated. The polarizabilities, shown in Fig. 3(b), reflect this behavior: While the larger target is consistently well predicted, the weaker one is better predicted at similar depth (see the dipping weak component for $dz = 25$ cm, indicating a sign change and thus a weak corresponding component of the secondary magnetic field).

In depth investigations of these cases suggested that the data set itself might not be totally consistent from grid point to grid point but contains variations that are likely at the origin of some of the errors in the inversion results. As a matter of fact, although the natural operating mode of the MPV is to be waved above the targets, the data provided to us have been collected in an inverted configuration, whereby the MPV was held fixed and the targets were moved on a 5×5 square grid with 20 cm separation between adjacent points. Repeatability between grid point therefore cannot be guaranteed since the two targets can easily move with respect to each other, either in distance or in orientation. Since our algorithm assumes an invariant configuration from grid point to grid point (akin to when the targets are buried), these errors would induce inversion inaccuracies. Yet, the overall good agreement between the inverted results and reported ground truth confirms the possibility of using the MPV for the detection and classification of multitargets.

B. TEMTADS Data

A systematic measurement campaign using the TEMTADS sensor has been undertaken by the Naval Research Laboratory
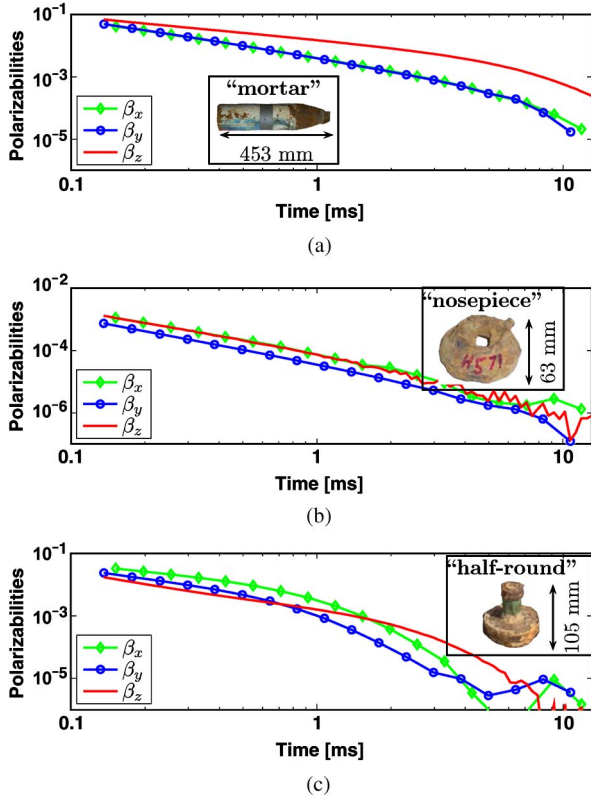
Fig. 4. Time-domain polarizabilities and inverted positions for three independent UXO using TEMTADS data. (a) Mortar. Inverted positions: $(-0.5, 0.6, 60.8)$ [cm]. True positions: $(0, 0, 60)$ [cm]. (b) Nose piece. Inverted positions: $(0.2, 0.2, 30.2)$ [cm]. True positions: $(0, 0, 30)$ [cm]. (c) Half round. Inverted positions: $(0.4, 0.1, 47.6)$ [cm]. True positions: $(0, 0, 49)$ [cm].

TABLE III
TRUE AND INVERTED POSITIONS OF TWO SIMULTANEOUS TARGETS WHOSE TIME-DEPENDENT POLARIZABILITIES ARE SHOWN IN FIG. 5(a) (TEMTADS DATA). GROUND TRUTH CORRESPONDS TO A FIXED MORTAR AND A MOVING NOSE PIECE ALONG THE $\hat{x}$ AXIS BY THE INDICATED dx WHILE KEEPING y AND z CONSTANTS. DEVIATIONS OF THE FIRST FEW CASES ARE DUE TO THE DIFFICULTY IN INVERTING ACCURATE POSITIONS WHEN THE TWO TARGETS ARE ON TOP OF EACH OTHER, WHEREAS DEVIATIONS OF THE LAST FEW CASES ARE EXPLAINED BY THE FACT THAT THE TARGET LOCATION EXTENDS BEYOND THE PHYSICAL SIZE OF THE SENSOR. ALL DIMENSIONS ARE IN CENTIMETERS, AND POSITIONS ARE ROUNDED TO THE CLOSEST INTEGER

	Mortar				Nose piece		
	x	y	z	dx	x	y	z
Truth	0	0	60	dx		0	30
Case							
1	-1	1	62	0	2	0	33
2	0	1	60	10	15	0	30
3	1	1	61	20	21	0	34
4	1	1	61	30	31	0	34
5	1	1	60	40	41	-1	34
6	0	1	61	50	51	0	32
7	1	1	60	60	60	0	33
8	0	1	60	70	67	0	31
9	0	1	60	80	75	0	31
10	0	1	60	90	79	0	33
11	0	1	60	100	80	0	39

on one, two, as well as three-target configurations. The targets of interest were a 4.2-in mortar, a nose cone, and a half round whose time-dependent polarizabilities are represented in Fig. 4 when they are inverted as separate targets. Like the 81 mm previously, the mortar exhibits a typical signature of a UXO, whereby one polarizability dominates the other two which are almost identical, indicating that the target is a BOR with a preferential direction. The nose piece produces a signal that is about two orders of magnitude inferior to the mortar, with a mostly log-log linear time decay indicating a strong ferrous component. In addition, the three polarizabilities are comparable which suggests a somewhat homogeneous shape in three directions, akin to a sphere. The half round produces a signal of comparable magnitude to the mortar with the strongest dipole switching in time from the $\hat{x}$ direction to the $\hat{z}$ direction. These signatures have been obtained using the method presented in the previous section and have been independently validated [36]. The inverted positions, listed in the captions of Fig. 4, match the true values with a centimeter accuracy and validate our algorithm as well as the associated TEMTADS model in the case of single targets. We emphasize also the fact that the inverted angles are typically within a few degrees of their expected values.

Two-target configurations consisted of combining the mortar with one of the other two targets and varying their respective lateral distances while keeping their depths constant. The lateral distances were varied from $x = 0$ cm to $x = 100$ cm at

10-cm intervals (yielding 11 configurations). At $x = 0$, the targets are immediately on top of each other, which is known to be a challenging configuration to invert due to the strong EMI signal decay. On the other hand, the position $x = 0$ is advantageous because the target is surrounded by sensors, and therefore, data carry information from multiple views around the targets. At $x = 100$ cm, however, the target is at the edge of the instrument and not immediately under a receiver. The amount of quality data is therefore limited in this case: Multi-looks around the target are not available, and many receivers are too far away to retain usable information. As a result, inversion results are expected to be best when targets are between the two extreme positions $x = 0$ and $x = 100$ cm.

A systematic inversion of all 11 configurations was carried out on both sets of measurements (mortar + nose piece and mortar + half round). The inverted positions for the first set are listed in Table III, and the time signatures are shown in Fig. 5(a). The results show the polarizabilities of the mortar practically identical for all 11 configurations, as expected, since the polarizabilities $\bar{\bar{\beta}}$ are an intrinsic property of the target, independent of its location and orientation. The polarizabilities of the nose piece present more variations, primarily due to the fact that some configurations correspond to a nose piece located close to either $x = 0$ or $x = 100$ cm. Nonetheless, all the signatures are seen to be linear and in good relationship with one another. The inverted positions of both targets remain within ± 1 cm accuracy for x between 20 and 60 cm, except for the depth of the nose piece whose error can amount to a few centimeters. The largest error, of about 9 cm, corresponds to the case when the lateral offset is $x = 100$ cm which brings the target at the edge of the instrument.

The results for the second set of measurements (mortar + half round), summarized in Table IV and Fig. 5(b), present more variations between the 11 configurations (note that the polarizabilities of the half round have been scaled by 10^{-2} in
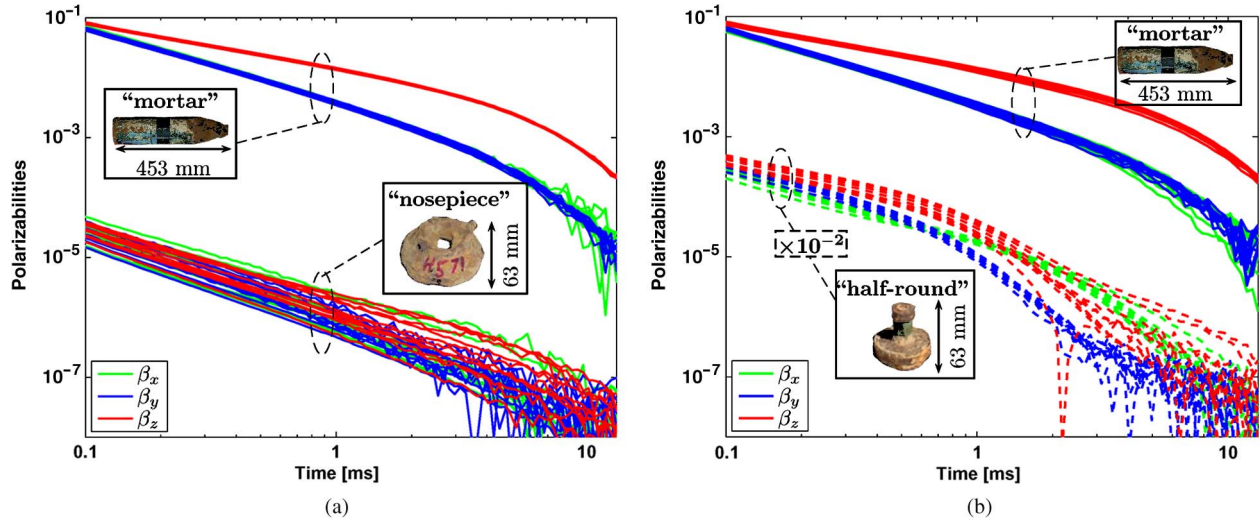
Fig. 5. Time-dependent polarizabilities for two-target inversions from TEMTADS data. The various cases correspond to various lateral displacements along $\hat{x}$ of the shallower target, while the deeper one (the mortar) is kept at a constant location. True and inverted positions are given in Tables III and IV. Note that the polarizabilities of the half round in (b) have been scaled by 10^{-2} in order to visually separate them from those of the mortar.

TABLE IV
TRUE AND INVERTED POSITIONS OF TWO SIMULTANEOUS TARGETS WHOSE TIME-DEPENDENT POLARIZABILITIES ARE SHOWN IN FIG. 5(b) (TEMTADS DATA). THE GROUND TRUTH CORRESPONDS TO A FIXED MORTAR AND A MOVING HALF ROUND ALONG THE $\hat{x}$ AXIS BY THE INDICATED dx WHILE KEEPING y AND z CONSTANTS. DEVIATIONS OF THE FIRST FEW CASES ARE DUE TO THE DIFFICULTY IN INVERTING ACCURATE POSITIONS WHEN THE TWO TARGETS ARE ON TOP OF EACH OTHER, WHEREAS DEVIATIONS OF THE LAST FEW CASES ARE EXPLAINED BY THE FACT THAT THE TARGET LOCATION EXTENDS BEYOND THE PHYSICAL SIZE OF THE SENSOR. ALL DIMENSIONS ARE IN CENTIMETERS, AND POSITIONS ARE ROUNDED TO THE CLOSEST INTEGER

	Mortar			Half round			
	x	y	z		x	y	z
Truth	0	0	60	dx		0	49
Case							
1	-4	1	53	0	-14	3	44
2	10	1	58	10	11	1	48
3	-1	1	56	20	26	1	47
4	1	1	58	30	32	1	48
5	1	0	59	40	41	1	48
6	1	0	59	50	50	0	48
7	1	0	60	60	59	0	47
8	1	0	60	70	67	0	47
9	1	0	60	80	73	0	47
10	0	0	60	90	80	0	49
11	0	0	60	100	89	0	51

TABLE V
TRUE AND INVERTED POSITIONS OF THREE SIMULTANEOUS TARGETS WHOSE TIME-DEPENDENT POLARIZABILITIES ARE SHOWN IN FIG. 6 (TEMTADS DATA). THE GROUND TRUTH CORRESPONDS TO A FIXED MORTAR, A FIXED HALF ROUND, AND A MOVING NOSE PIECE ALONG THE $\hat{x}$ AXIS BY THE INDICATED dx WHILE KEEPING y AND z CONSTANT. ALL DIMENSIONS ARE IN CENTIMETERS, AND POSITIONS ARE ROUNDED TO THE CLOSEST INTEGER

	Mortar			Half round			Nose piece			
	x	y	z	x	y	z	dx	x	y	z
Truth	0	0	60	50	0	49	dx		0	30
Case										
1	2	0	61	50	0	47	0	0	0	36
2	2	1	58	50	0	47	10	14	0	31
3	2	0	59	50	0	47	20	22	1	31
4	2	1	59	51	0	47	30	28	1	34
5	2	1	60	55	1	47	40	37	1	36
6	1	1	59	50	1	49	50	49	0	38
7	3	1	59	42	1	50	60	58	0	36
8	1	1	59	50	0	46	70	81	3	27
9	2	1	59	48	1	48	80	84	0	32
10	2	1	59	47	0	48	90	83	0	38
11	2	1	60	55	0	43	100	-	-	-

order to separate them from those of the mortar). The signature of the mortar, although still clearly separated into a strong component and two smaller identical ones, exhibits fluctuations larger than in the previous case but not substantial enough to hinder a proper identification of this target. The polarizabilities of the half round also show a flipping dipole behavior between $\hat{x}$ in early time and $\hat{z}$ in late time, albeit somewhat smoothed out in the fluctuations between all the 11 configurations. Note again that fluctuations in the signature of the second object are expected due to its varying position which reaches the extremity of the sensor in some cases.

A series of 11 three-target configurations were analyzed whereby two targets were fixed and one was moving from case to case. The stationary targets were the mortar held horizontally at $(x, y, z) = (0, 0, 60)$ [cm] and the half round held horizon-

tally at $(x, y, z) = (50, 0, 49)$ [cm]. The moving target was the nose piece held vertically at $(x, y, z) = (dx, 0, 30)$ [cm] with dx varying from 0 to 100 cm in increments of 10 cm. The recovered positions for these configurations are summarized in Table V and show an overall good agreement with the ground truth. The two stationary targets are well located in the (xy) plane, and the depths are typically estimated within a centimeter for the mortar and within a couple of centimeters for the half round, except again in a few isolated cases that correspond for the most part to targets at the edge of the instrument. The positions of the nose piece present more fluctuations while still following the ground truth reasonably well in the majority of cases. The most problematic positions are still those corresponding to the target being at the limit of the field of view of the instrument where an error up to 9 cm in lateral position and 8 cm in depth is recorded. The time-dependent polarizabilities, shown in Fig. 6, confirm these conclusions. The mortar as well as the half round presents very consistent signatures from case to case. Interestingly, the signatures of the half round are more consistent than in the
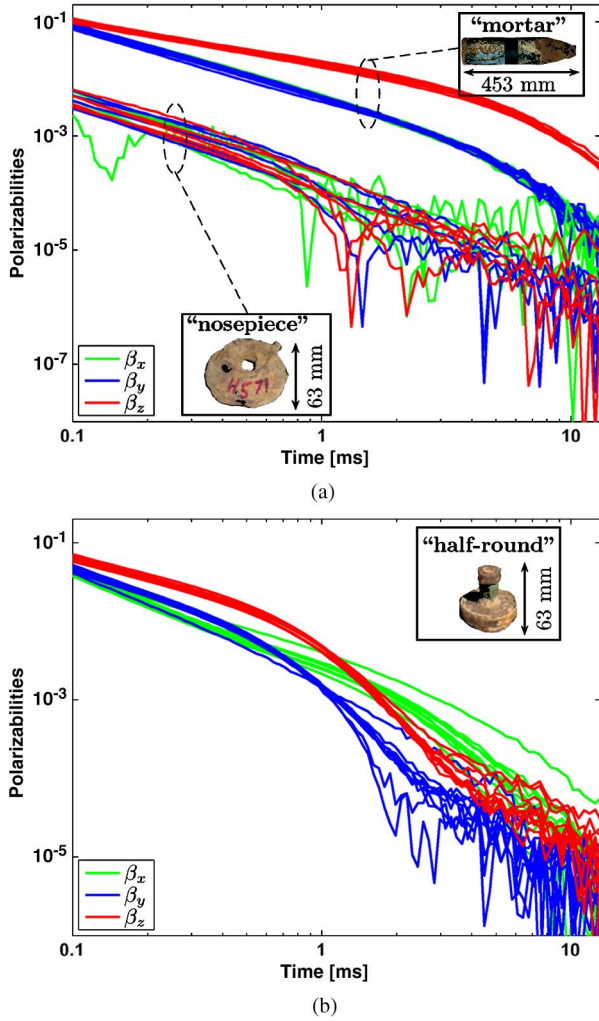
Fig. 6. Three-target inversions from TEMTADS data. The mortar and the half round are held fixed at $(x, y, z) = (0, 0, 60)$ [cm] and $(x, y, z) = (50, 0, 49)$ [cm], respectively, while the nose piece moves along $\hat{x}$ from case to case. True and inverted positions are given in Table V. (a) Mortar and nose piece. (b) Half round.

two-target inversions of Fig. 5(b), primarily due to the larger lateral separation with the mortar (50 cm in this case). The polarizabilities of the nose piece are a few orders of magnitude lower than those of the mortar and half round but with much more variations from case to case. We again attribute these to two main reasons: overlapping targets and edge effects. Edge effects refer to the effect already witnessed, by which the inverted position and time-domain polarizabilities of a target located at the edge of the instrument can present large errors. It is therefore expected that the region close to $x = 100$ cm is a source of inaccurate polarizabilities. The overlapping target effect refers to the fact that EMI signatures are intrinsically challenging to separate for targets in proximity and on top of each other. In this particular set of measurements, the nose piece travels from $x = 0$ to $x = 100$ cm and is directly on top of targets at $x = 0$ (the mortar) and $x = 50$ cm (the half round). A case by case examination reveals that the position $x = 0$ is well inverted and that the polarizabilities exhibit the expected linear decay (on a log-log scale) depicted for example in Fig. 5(a). The polarizabilities when the nose piece is close

to $x = 50$ cm, however, present much more variation and can be seen in Fig. 6(a). The major difference between the two situations are the distances between the targets when they coincide laterally: 30 cm in one case and about 20 cm in the other. It is expected that allowing variations in $\hat{y}$ for target positions would significantly improve the results. Note also that, in all cases, including those challenging ones, the inverted positions remain within reasonable bounds.

V. DISCUSSION AND CONCLUSION

The Gauss–Newton-based algorithm presented in this paper has been shown to be effective at simultaneously inverting the positions, orientations, and time-dependent polarizabilities of multiple UXO within the field of view of EMI sensors. Part of the efficiency is due to the construction of the unknown vector, in which the positions and orientations of the targets' equivalent dipoles are assumed time independent and inverted for only once using the information of all time channels. Another important aspect of the algorithm is that it is largely based on an analytical derivation of the Jacobian matrix, which therefore provides exact derivatives of the secondary magnetic field with respect to all unknown quantities while reducing the computation time.

Inherent to the method itself, various initial guesses to seed the algorithm and maximum iteration numbers have been tested, depending on the complexity of the cases studied. For single targets, ten iterations were, in general, sufficient, whereas up to 200 iterations were run for three-target cases. An increased number of iterations naturally result in an increased computation time, which reached almost 3 min in the case of TEMTADS data inverted on three targets (we recall that the TEMTADS data set is typically much larger than the MPV data set so that inversions are more time consuming). The final solution produced by the algorithm is remarkably insensitive to the initial guess (apart from obvious divergences), provided that the step at each iteration is weighted by a parameter $0 < \alpha < 1$. A value of $\alpha = 0.5$ yielded very consistent inverted positions in all examples shown despite large variations in initial guesses: within ± 50 cm for both x and y coordinates and between -50 cm and -20 cm for the depths. The inverted polarizabilities, however, were more sensitive particularly in the three-target cases yet still within acceptable bounds. To resolve possible variations, the algorithm was run on typically ten realizations. The selection of the final solution was performed by using two often corroborating criteria. First, the histogram of solutions for the inverted positions was examined, and the most frequent solution was declared final. Second, the error was computed between the measured and computed fields, and the solution that produced the lowest error was declared final. In all cases considered, these two criteria selected identical solutions. It should also be mentioned that simpler cases such as single target inversion yielded similar final solutions in almost all the cases, so that the criteria proposed earlier were mostly useful when inverting multitarget configurations.

Finally, we emphasize that the assumption of a known number of targets [i.e., known N in (4)] is necessary for the development of the algorithm but is not required in practice,

and only the knowledge of an upper bound is needed. If the algorithm is run with N larger than the actual number of targets, the algorithm may yield two types of results. First, some dipoles cluster around a certain location and capture the secondary field of a given UXO better than a single dipole. This situation is not very common but can occur for very heterogeneous targets. More commonly, clusters are very tight, and the dipoles find themselves practically at the same location. The corresponding time-dependent polarizabilities need to be added and collectively represent the signature of the target (individual polarizabilities typically do not exhibit any physical behavior). The second type of results obtained if N is larger than the actual number of targets is that some dipoles converge to apparently irrelevant locations, with polarizabilities at a few orders of magnitude lower than those of the targets themselves. We attribute this behavior to the algorithm's attempt to find a best fit for noisy data, which is obtained with a few well-identified dipoles and other weaker ones that capture average noise contributions. At the target identification stage, these spurious dipoles are easily filtered out due to their unphysical and weak responses. Note also that this latter behavior precludes the use of the misfit error to determine the number of targets since smaller errors are typically obtained with more dipoles. Consequently, the algorithm does not require the exact knowledge of the number of targets for their proper identification, and only an upper bound needs to be estimated. This topic is currently under investigation.

ACKNOWLEDGMENT

REFERENCES

[1] K. O'Neill, S. Haider, S. Geimer, and K. Paulsen, "Effects of the ground surface on polarimetric features of broadband radar scattering from subsurface metallic objects," *IEEE Trans. Geosci. Remote Sens.*, vol. 39, no. 7, pp. 1556–1565, Jun. 2001.

[2] K. O'Neill, "Discrimination of UXO in soil using broadband polarimetric GPR backscatter," *IEEE Trans. Geosci. Remote Sens.*, vol. 39, no. 2, pp. 356–367, Feb. 2001.

[3] C. E. Baum, *Detection and Identification of Visually Obscured Targets*. Philadelphia, PA: Taylor & Francis, 1999.

[4] J. D. Jackson, *Classical Electrodynamics*, 3rd ed. Hoboken, NJ: Wiley, 1999.

[5] T. H. Bell, B. J. Barrow, and J. T. Miller, "Subsurface discrimination using electromagnetic induction sensors," *IEEE Trans. Geosci. Remote Sens.*, vol. 39, no. 6, pp. 1286–1293, Jun. 2001.

[6] Y. Zhang, L. Collins, H. Yu, C. Baum, and L. Carin, "Sensing of unexploded ordnance with magnetometer and induction data: Theory and signal processing," *IEEE Trans. Geosci. Remote Sens.*, vol. 41, no. 5, pp. 1005–1015, May 2003.

[7] C. O. Ao, H. Braunisch, K. O'Neill, and J. A. Kong, "Quasi-magnetostatic solution for a conducting and permeable spheroid with arbitrary excitation," *IEEE Trans. Geosci. Remote Sens.*, vol. 40, no. 4, pp. 887–897, Apr. 2002.

[8] B. E. Barrowes, K. O'Neill, T. M. Grzegorczyk, X. Chen, and J. A. Kong, "Broadband analytical magnetoquasistatic electromagnetic induction solution for a conducting and permeable spheroid," *IEEE Trans. Geosci. Remote Sens.*, vol. 42, no. 11, pp. 2479–2489, Nov. 2004.

[9] T. M. Grzegorczyk, B. Zhang, J. A. Kong, B. E. Barrowes, and K. O'Neill, "Electromagnetic induction from highly permeable and conductive ellipsoids under arbitrary excitation-application to the detection of unexploded ordinances," *IEEE Trans. Geosci. Remote Sens.*, vol. 46, no. 4, pp. 1164–1176, Apr. 2008.

[10] F. Shubitidze, K. O'Neill, B. Barrowes, I. Shamatava, K. Sun, J. P. Fernandez, and K. D. Paulsen, "Application of the normalized surface magnetic charge model to UXO discrimination in cases with overlapping signals," *J. Appl. Geophys.*, vol. 61, no. 3/4, pp. 292–303, Mar. 2007.

[11] C. D. Moss, T. M. Grzegorczyk, K. O'Neill, and J. A. Kong, "A hybrid time domain model of electromagnetic induction from conducting, permeable targets," *IEEE Trans. Geosci. Remote Sens.*, vol. 44, no. 10, pp. 2916–2926, Oct. 2006.

[12] S. L. Tantum and L. M. Collins, "A comparison of algorithms for subsurface target detection and identification using time-domain electromagnetic induction data," *IEEE Trans. Geosci. Remote Sens.*, vol. 39, no. 6, pp. 1229–1306, Jun. 2001.

[13] X. Chen, K. O'Neill, T. M. Grzegorczyk, and J. A. Kong, "Spheroidal mode approach for the characterization of metallic objects using electromagnetic induction," *IEEE Trans. Geosci. Remote Sens.*, vol. 45, no. 3, pp. 697–706, Mar. 2007.

[14] F. Shubitidze, J. P. Fernández, B. E. Barrowes, I. Shamatava, and K. O'Neill, "Normalized surface magnetic source model applied to Camp Sibert data sets: Discrimination studies," in *Proc. 25th Int. Rev. Progress Appl. Comput. Electromagn.*, Monterey, CA, Mar. 8–12, 2009.

[15] J. P. Fernández, F. Shubitidze, I. Shamatava, B. E. Barrowes, and K. O'Neill, "Realistic subsurface anomaly discrimination using electromagnetic induction and an SVM classifier," *EURASIP J. Adv. Signal Process.*, vol. 210, p. 305 890, Jan. 2010.

[16] I. T. McMichael and C. V. Nelson, "Investigation of the electromagnetic induction spatial response of two closely spaced targets," in *Proc. SPIE*, Orlando, FL, 2003, vol. 5089, pp. 894–903.

[17] K. O'Neill, K. Sun, C. C. Chen, F. Shubitidze, and K. D. Paulsen, "Combining GPR and EMI data for discrimination of multiple subsurface metallic objects," in *Proc. IEEE Int. Geosci. Remote Sens. Symp.*, 2003, vol. 7, pp. 4157–4159.

[18] K. Sun, K. O'Neill, C. C. Chen, F. Shubitidze, and K. D. Paulsen, "Highly contaminated UXO sites: Combination of GPR and EMI for discrimination of clustered scatterers," in *Proc. SAGEEP*, Atlanta, GA, 2005, pp. 1156–1165.

[19] W. Hu, S. L. Tantum, and L. M. Collins, "EMI-based classification of multiple closely spaced subsurface objects via independent component analysis," *IEEE Trans. Geosci. Remote Sens.*, vol. 42, no. 11, pp. 2544–2554, Nov. 2004.

[20] C. S. Throckmorton, S. L. Tantum, Y. Tan, and L. M. Collins, "Independent component analysis for UXO detection in highly cluttered environments," *J. Appl. Geophys.*, vol. 61, no. 3/4, pp. 304–317, Mar. 2007.

[21] L.-P. Song, D. W. Oldenburg, L. R. Pasion, and S. D. Billings, "Transient electromagnetic inversion for multiple targets," in *Proc. SPIE*, May 2009, vol. 7303, p. 730 30R.

[22] A. J. Devaney, "Time reversal imaging of obscured targets from multistatic data," *IEEE Trans. Antennas Propag.*, vol. 53, no. 5, pp. 1600–1610, May 2005.

[23] F. Shubitidze, B. Barrowes, I. Shamatava, and K. O'Neill, "Multiple subsurface target localization from next generation EMI sensor data using MUSIC algorithm," presented at IGARSS, 2010.

[24] Y. Zhong and X. Chen, "MUSIC imaging and electromagnetic inverse scattering of multiply scattering small anisotropic spheres," *IEEE Trans. Antennas Propag.*, vol. 55, no. 12, pp. 3542–3549, Dec. 2007.

[25] T. M. Grzegorczyk, B. Barrowes, F. Shubitidze, J. P. Fernandez, I. Shamatava, and K. O'Neill, "Kalman filters applied to the detection of unexploded ordnance," in *Proc. SPIE—Detection and Sensing of Mines, Explosive Objects, and Obscured Targets*, Orlando, FL, 2010, vol. 7664.

[26] T. M. Grzegorczyk, B. Barrowes, F. Shubitidze, J. P. Fernandez, I. Shamatava, and K. O'Neill, "Detection of multiple subsurface metallic targets using EMI data," in *Proc. SPIE—Detection and Sensing of Mines, Explosive Objects, and Obscured Targets*, Orlando, FL, 2009, vol. 730 30T.

[27] H. H. Nelson and J. R. McDonald, "Multi-sensor towed array detection system (mtads) for UXO detection," *IEEE Trans. Geosci. Remote Sens.*, vol. 39, no. 6, pp. 1139–1145, Jun. 2001.

[28] H. H. Nelson, D. A. Steinhurst, B. Barrow, T. Bell, N. Khadar, B. SanFilipo, and I. J. Won, "Enhanced UXO discrimination using frequency-domain electromagnetic induction," Naval Res. Lab., Washington, DC, A398964, 2007, final report to the ESTCP program office (DOD) Arlington VA for project MM-0601, Accession No. ADA469893.

[29] [Online]. Available: http://www.serdp.org/Research/upload/UX-1443-fs.pdf

[30] J. Stratton, *Electromagnetic Theory*. New York: McGraw-Hill, 1941. 0-07-062150-0.

[31] F. Shubitidze, K. O'Neill, S. A. Haider, K. Sun, and K. D. Paulsen, "Application of the method of auxiliary sources to the wide-band electromagnetic induction problem," *IEEE Trans. Geosci. Remote Sens.*, vol. 40, no. 4, pp. 928–942, Apr. 2002.

[32] F. Shubitidze, K. O'Neill, I. Shamatava, and K. Sun, "Coupling between highly conducting and permeable metallic objects in the emi frequency range," *Appl. Comput. Electromagn. Soc. J.*, vol. 19, no. 1, pp. 139–148, Mar. 2004.

[33] H. Braunisch, C. O. Ao, K. O'Neill, and J. A. Kong, "Magnetoquasistatic response of a distribution of small conducting and permeable objects," in *Proc. IEEE Int. Geosci. Remote Sens. Symp.*, 2000, pp. 1424–1426.

[34] F. Shubitidze, K. O'Neill, I. Shamatava, K. Sun, and K. D. Paulsen, "A standardized excitation approach for classification of buried UXO," in *Proc. IEEE Int. Geosci. Remote Sens. Symp.*, 2004, vol. 7, pp. 4905–4908.

[35] J. Miller, "Classification using electromagnetic induction sensors," in *Proc. UXO Forum*, Orlando, FL, Aug. 24–27, 2009.

[36] F. Shubitidze, D. Karkashadze, J. P. Fernandez, B. E. Barrowes, K. O'Neill, T. M. Grzegorczyk, and I. Shamatava, "Applying a volume dipole distribution model to next-generation sensor data for multi-object data inversion and discrimination," in *Proc. SPIE*, 2010, p. 766407.

Tomasz M. Grzegorczyk (SM'07) received the Ph.D. degree from the Laboratoire d'Electromagnetisme et d'Acoustique, Ecole Polytechnique Federale de Lausanne (Swiss Federal Institute of Technology), Lausanne, Switzerland, in 2000.

From January 2001 to July 2007, he was a Research Scientist with the Research Laboratory of Electronics, Massachusetts Institute of Technology (MIT), Cambridge, and a Research Affiliate with MIT until January 2011. In 2007, he founded Delpsi, LLC, where he continues performing unclassified research for the Department of Defense, as well as various companies and universities. He is an Adjunct Professor at Zhejiang University, Hangzhou, China. He has recently authored a book on metamaterials. His research interests include the use of electromagnetic induction for the detection and classification of unexploded ordnance, biomedical microwave imaging, optical binding and trapping, wave propagation in bianisotropic media, and left-handed metamaterials.

Dr. Grzegorczyk is a member of the Optical Society of America. He has served as an Editor and board member of two international peer-reviewed journals (*The Progress In Electromagnetic Research* and the *Journal of Electromagnetic Waves and Applications*) and one international conference (The Progress in Electromagnetics Research Symposium).

Benjamin E. Barrowes (S'98–M'04) received the B.S. and M.S. degrees in electrical engineering from Brigham Young University, Provo, UT, in 1999 and the Ph.D. degree from the Massachusetts Institute of Technology (MIT), Cambridge, in 2004.

During 2004–2005, he was a Director's funded Postdoc at Los Alamos National Laboratory in the Physics Division. He is currently a Physicist with the Cold Regions Research and Engineering Laboratory, Engineer Research and Development Center, Hanover, NH. His research interests center on electromagnetic wave theory and modeling with applications including wind-wave interaction, electromagnetic scattering from the sea surface as well as from random media, nanoscale energy generation techniques, computer interface methodologies, electromagnetic induction models for nonspherical geometries, and biological electromagnetic phenomena. Other interests include automatic code conversion/translation and arbitrary precision computing.

Dr. Barrowes was named the top high school math student in the state of Utah (1991), received two Rocky Mountain Space Grant Consortium grants, and was awarded a National Science Foundation graduate fellowship.

Fridon Shubitidze (A'98–M'04) received the degree of Diploma radio physicist (M.S.) from the Sukhumi branch of Tbilisi State University (TSU), Sukhumi, Republic of Georgia, in 1994 and the Cand.Sci. (Ph.D.) degree in radio physics (applied electromagnetics) from TSU in 1997.

In 1994, he was a Member of the Research Staff of the Laboratory of Applied Electrodynamics, Department of Physics, TSU. At the same time, he was with the Department of Physics and Mathematics, Sukhumi branch of TSU, as a Senior Teacher and became an Associate Professor in 1998. From 1998 to 1999, he was a Postdoctoral Fellow with the National Technical University of Athens, Athens, Greece, performing research in connection with computer simulation of electrostatic discharge, electrodynamic aspects of electromagnetic compatibility, numerical modeling of conformal antennas, electromagnetic wave scattering, field visualization and identification of objects by scattered field analysis, investigation of wave propagation through anisotropy, plasma, and chiral media, and innovative numerical methods. From June to August 2005, he was a Visiting Scientist at the Department of Earth and Ocean Science, University of British Columbia, Vancouver, BC, Canada. He is currently a Research Professor with the Thayer School of Engineering, Dartmouth College, Hanover, NH. His current work interests focus on numerical modeling of forward and inverse electromagnetic scattering by subsurface metallic objects, investigation of global magnetoquasistatic fields due to ionospheric currents, and electrostatic fields' effects on robotic and construction systems for Mars and Lunar exploration.

Juan Pablo Fernández received the degree of Físico from the Universidad de los Andes, Bogotá, Colombia, in 1990, the Ph.D. degree in theoretical low-temperature physics from the University of Massachusetts Amherst, Amherst, in 2004, and the M.S. degree in engineering sciences from the Thayer School of Engineering, Dartmouth College, Hanover, NH, in 2007.

He has taught physics, mathematics, astronomy, Spanish, and scientific writing with the Universidad de los Andes, the University of Massachusetts, Amherst College, Amherst, MA, Smith College, Northampton, MA, and Lebanon College, Lebanon, NH. He has worked as a writer, editor, and translator, and managed the processing of grant proposals for the Instituto Colombiano para el Desarrollo de la Ciencia y la Tecnología, "Colciencias." He has also been a Research Associate with the Thayer School of Engineering and is, at present, a Research Consultant with the Electromagnetic Sensing Group, Thayer School of Engineering, and with the Cold Regions Research and Engineering Laboratory, Engineer Research and Development Center, Hanover, NH. His current research involves the discrimination of unexploded ordnance using electromagnetic induction methods and machine learning.

Dr. Fernández is a member of the Applied Computational Electromagnetics Society. He was the recipient of a "Francisco de Paula Santander" grant for creative writing by the Instituto Colombiano de Cultura in 1990, was shortlisted for the Premio Nacional de Literatura in 1998, and received the Eugene M. Isenberg Award from the Isenberg School of Management at the University of Massachusetts in 1997 and 1998.

Kevin O'Neill (M'98) received the B.A. degree (*magna cum laude*) from Cornell University, Ithaca, NY, and the M.A. and M.S.E. degrees in 1974 and Ph.D. degree in 1978, from Princeton University, NJ, respectively.

After a National Science Foundation Postdoctoral Fellowship at the Thayer School of Engineering, Dartmouth College, Hanover, NH, and the U.S. Army Cold Regions Research and Engineering Laboratory (CRREL), he was with CRREL as a Research Civil Engineer. His research has focused on numerical modeling of porous media transport phenomena and of geotechnically relevant electromagnetic problems. He has been a Visiting Fellow at the Department of Agronomy, Cornell University, a Visiting Scientist at the Center for Electromagnetic Theory and Applications, Massachusetts Institute of Technology, Cambridge, and since 1984, he has been on the adjunct faculty of the Thayer School of Engineering. His current work centers on electromagnetic remote sensing of surfaces, layers, and particularly buried objects such as unexploded ordnance.